

Profiling THz Beams With Off-Label Use of Infrared Microbolometric Cameras

Gabriel Nagamine,¹ Carlo Vicario,² Tariq Leinen,¹ Guy Matmon,² Marco Raffa,³ Mattias Beck,³ Giacomo Scalari,³ Adrian L. Cavalieri,^{1,2} Flavio Giorgianni^{1,2}

¹*Institute of Applied Physics, University of Bern, CH-3012 Bern, Switzerland*

²*Paul Scherrer Institute, CH-5232 Villigen-PSI, Switzerland*

³*Institute for Quantum Electronics, Department of Physics, ETH Zürich, CH-8093 Zurich, Switzerland*

Abstract— Visualizing the spatial profile of light beams is essential for evaluating irradiance, characterizing beam quality, and achieving precise alignment. In the optical spectral range, this is readily performed using silicon-based CCD and CMOS cameras. In the terahertz (THz) range, however, it typically requires specialized detectors with prohibitive costs. Here, we show that an infrared (IR) camera can be used outside of its labeled specifications to achieve similar performance as a dedicated microbolometric THz camera, at under 1% of the THz camera's cost. We compared the cameras by characterizing THz beam profiles from two sources: a pulsed broadband THz beam produced through optical rectification in organic crystals, and a narrowband quasi-continuous-wave (quasi-CW) THz beam emitted by a quantum cascade laser. For the broadband THz radiation, the beam width measured by the two cameras differed by only ~6%, well within the pixel resolution limit, and in the narrowband quasi-CW case by just ~1.3%. Additionally, the IR camera exhibits a lower minimum detectable power (down to 1.5 THz) than the THz camera, while also maintaining a linear and polarization-independent responsivity. These results expand the applicability of conventional IR cameras to the THz range, suggesting that they will become routine tools for high-fidelity THz beam diagnostics and imaging in scientific and industrial applications.

Index Terms—microbolometer, organic crystal, quantum cascade laser, terahertz detector, terahertz imaging

Beam profiling is a standard routine in optics, as it quantifies the spatial intensity distribution, enabling precise alignment in applications ranging from laser machining to imaging and spectroscopy [1]. From the infrared to ultraviolet range, beam profiling is routinely performed using semiconductor-based CCD/CMOS cameras [2]. In these cameras, photons in the electron-volt range excite electron-hole pairs to generate an appreciable electronic signal. However, such devices are not

directly applicable in the terahertz (THz) regime, where the photon energies are comparable to thermal energy at room temperature. As a result, direct photon detection of THz radiation requires cryogenic cooling.

To overcome the need for cryogenic cooling, commercial manufacturers of THz cameras have explored different detection principles. For instance, companies like Terasense offer cameras where the THz radiation is detected by the direct excitation of plasma oscillations in a two-dimensional electron system. While this approach is highly effective in the sub-THz regime, these devices often rely on the use of resonant structures that limit the sensitivity at frequencies above 1 THz [3]. Alternatively, other technologies rely on thermal detection, where the incident radiation is absorbed and converted into heat, causing a measurable change in the detectors' physical properties [4]. This category includes pyroelectric arrays, offered by companies such as Ophir, which measure temperature-induced changes in electrical polarization [5]. However, as this method is only sensitive to temperature variations, it requires the use of schemes with mechanical optical choppers to image continuous-wave (CW) or quasi-CW sources. To address these limitations, microbolometric focal-plane arrays, offered by companies such as NEC or INO, are currently one of the most widely used sensors in state-of-the-art THz cameras. These detectors uniquely combine room-temperature operation with two-dimensional imaging, do not require optical chopping, and provide sufficient sensitivity for real-time imaging [6-8] of practical THz sources [3-5, 9].

Microbolometers, however, are not exclusive to the THz domain. The same thermal detection principle underpins inexpensive, mass-produced infrared (IR) thermal cameras, which benefit from CMOS-compatible fabrication, mature industrial processes, and large-scale production [10]. While THz and IR microbolometers exploit the same fundamental operating principles, they differ substantially in optical coupling strategies, absorber design, and pixel geometry, which are nominally optimized for distinct wavelength ranges and fabrication scales [3]. These engineering differences and

Corresponding Authors

E-mails: flavio.giorgianni@unibe.ch, gabriel.nagaminegomez@unibe.ch

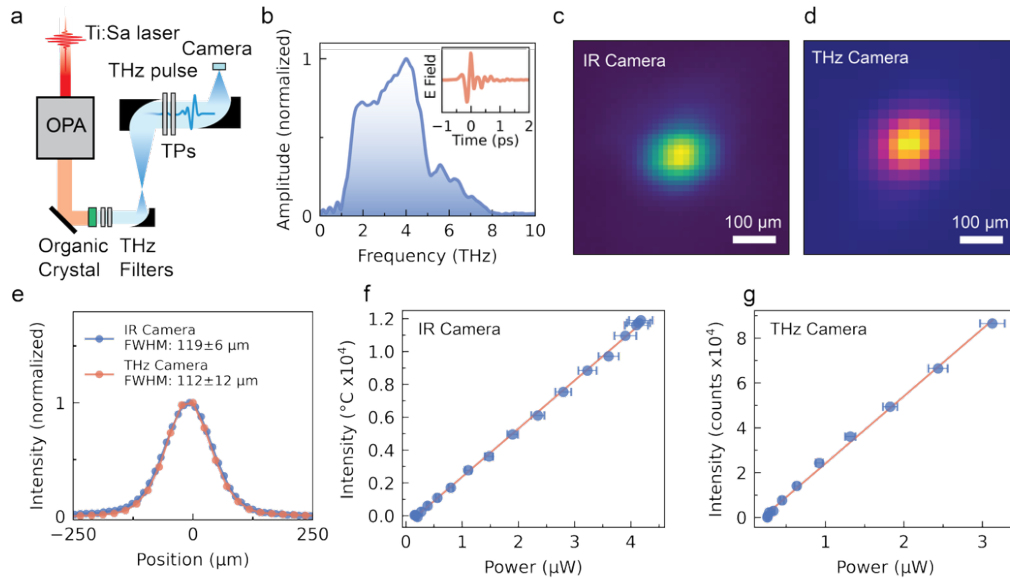


Fig. 1 Comparison between THz and IR cameras for THz detection. (a) Schematic of the THz beam profiling setup. The signal beam from an optical parametric amplifier (OPA) is optically rectified in a DSTMS organic crystal, generating broadband THz radiation (1-8 THz). To avoid leakage of the fundamental, three low-pass THz filters, two with cutoff frequencies of 20 THz, and the other with a cutoff frequency of 10 THz, are inserted in the THz beam. The THz beam is then focused on the cameras, after passing through two THz polarizers (TPs) to control the incident power. (b) THz amplitude spectrum obtained through electro-optic sampling of the THz electric field in the time domain (shown in the inset). (c-d) Image of the focused THz beam profile on the IR and THz cameras. Note that distinct colormaps are used to visually differentiate the two devices. (e) Comparison of horizontal cross-cuts obtained from the measured intensity profiles in (c, d). (f-g) Linearity of the signal strength as a function of THz irradiance. The x axes correspond to the average power, while the y axes report the raw integrated signal given by the cameras. Note that for the IR camera, the reported temperature corresponds to the spatially integrated pixel signal (sum over the beam area) and does not represent an actual thermodynamic temperature, whereas the THz camera output is given in counts.

production scale largely set the differences in cost and availability between THz and IR microbolometric cameras.

If IR microbolometric cameras could be proven useful in the THz – beyond their design specifications – they would be an attractive alternative to dedicated THz cameras. In this direction, a previous proof-of-concept study [11] has suggested that the dominant differences in detection sensitivity due to wavelength (THz vs. IR) are not intrinsic to the microbolometric sensing mechanism. Rather, they appear to arise primarily from different analog-to-digital conversion electronics and from the specific implementation of dynamic background-subtraction algorithms. However, the study described in Ref. [11] was limited to the spectral content below 2.5 THz, and key performance parameters, such as linearity, responsivity, and spectral sensitivity, were not fully explored.

In this paper, the linearity, spectral and polarization-dependent sensitivities, noise spectral density, and beam profiling capabilities of two commercially available microbolometric cameras that employ vanadium oxide (VOx) as the thermoresistive sensing material are evaluated and compared. Similar performance between the HIKMICRO Mini2PlusV2 IR camera (sold at ~\$249) and the NEC IR/V-T0831 THz camera (sold at ~\$30,000) is observed under both broadband THz and narrowband THz illumination. These results indicate that IR microbolometric cameras can indeed be used to accurately capture the THz radiation, offering an

affordable solution for THz imaging and beam profiling for research and industrial applications.

The first set of comparative measurements is performed using a focused broadband THz beam generated by laser-driven optical rectification in organic crystals. It should be noted that for clarity, the HIKMICRO Mini2PlusV2 camera will be referred to as the “IR camera” and the NEC IR/V-T0831 as the “THz camera”. Additionally, in all measurements with the IR camera, the IR collection lens was removed to allow direct illumination of the microbolometric array. This is required as common IR lens materials, such as doped germanium and chalcogenide glasses, do not transmit THz radiation [11-13].

A sketch of the experimental setup used to characterize the cameras under broadband THz illumination is shown in Fig. 1a. A 1 kHz Ti:Sapphire femtosecond laser system coupled to an optical parametric amplifier (OPA) delivers a 1.35 μm pulse, which is optically rectified in a DSTMS [14] or PNPA [15] organic crystal to generate collimated broadband THz radiation. Fig. 1b shows the THz amplitude spectrum, which is centered around 4 THz and extends between 0.3 and 8 THz. The spectrum is obtained from the Fourier amplitude of the THz pulse waveform (inset of Fig. 1b), which is measured by electro-optic sampling (EOS), as described in Section S1 of the Supplementary Material. After generation, the THz beam is isolated using sets of low-pass filters. It then propagates through a set of polarizers to adjust the transmitted power.

Finally, the beam is expanded and tightly focused (numerical aperture, $NA \sim 0.36$) into the cameras with three off-axis parabolic mirrors. Additional experimental details, including IR camera data handling, are reported in Section S1 of the Supplementary Material.

Images of the focused THz beam at an average intensity of 7 mW/cm^2 , acquired using the IR and THz cameras, are shown in Fig. 1c and Fig. 1d, respectively. Both images are shown after background subtraction and normalization. Horizontal cross-cuts of the intensity profiles are shown in Fig. 1e. Qualitatively, the two cameras capture nearly identical spatial beam distributions.

Quantitatively, the full-width at half-maximum (FWHM) is $119 \pm 6 \mu\text{m}$ for the IR camera and $112 \pm 12 \mu\text{m}$ for the THz camera, corresponding to a relative difference of only $\sim 6\%$. The uncertainty in the FWHM is estimated as half of the pixel pitch of each detector ($12 \mu\text{m}$ for the IR camera and $23.5 \mu\text{m}$ for the THz camera), indicating that the observed discrepancy is well within the spatial sampling limit of the sensors. The close agreement with the benchmark THz camera confirms that the IR camera can accurately resolve the THz beam profile.

In general, THz cameras employ larger pixels to increase the absorber area and enhance responsivity at long wavelengths [7, 16]. While both pixel pitches are smaller than the THz wavelength ($\sim 74 \mu\text{m}$ at 4 THz), finer sampling provided by the smaller pixels of the IR camera can, in principle, enable improved spatial resolution.

To verify the polarization dependence of the detector response, measurements were performed using linearly polarized THz radiation with horizontal and vertical polarization orientations (see Section S1 of the Supplementary Material). For both cameras, the relative deviation in the integrated signal between polarization states was approximately 0.3%, confirming the isotropic response of both detectors (Supplementary Table 1). While the thermal detection mechanism of microbolometers is, in principle, insensitive to the polarization of the incident radiation, the pixel geometry—particularly in designs incorporating antenna or resonant coupling structures—can introduce anisotropic or polarization-dependent responses. The negligible differences observed here indicate that the internal detector architecture does not introduce measurable polarization-dependent sensitivity in the investigated cameras. This polarization-insensitive response is particularly desirable for beam profiling and imaging applications, where the polarization state of the incident THz radiation may vary or be unknown.

The linearity in the response of the IR camera is also compared to the benchmark THz camera. Figs. 1f and 1g show the integrated image intensity as a function of the total incident THz average power (see Supplementary Material for details). The THz power is varied using two THz polarizers in series before the imagers. Both cameras exhibit nearly perfect linear response over the full range of intensities. A linear regression yields a slope of $2.9 \times 10^3 \text{ }^\circ\text{C}/\mu\text{W}$ for the IR camera and $3.0 \times 10^4 \text{ counts}/\mu\text{W}$ for the THz camera, with relative standard error of the slope of 0.7 and 1.7%, respectively.

Because the IR camera is operating outside its labeled specifications, its software natively reports the detected radiation as a temperature reading ($^\circ\text{C}$), whereas the dedicated THz camera outputs raw intensity counts. In the present off-label use of the IR camera for THz detection, the reported temperature therefore serves as a proportional measure of incident THz intensity.

A key parameter in validating the use of infrared (IR) cameras for beam profiling is the spectral range over which these devices operate reliably. To determine the operational range, the responsivity R and the sensitivity of both detectors were evaluated as a function of the incident THz frequency. To vary the incident THz spectral content, a set of low-pass THz filters with progressively lower cut-off frequencies was used.

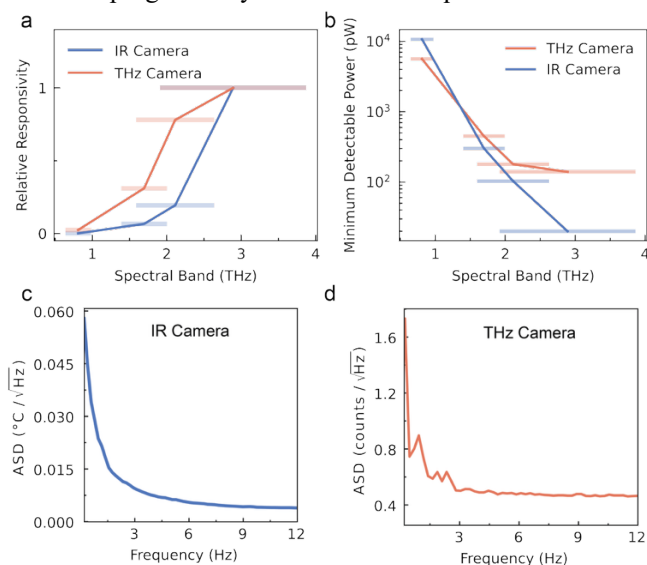


Fig. 2 Spectral dependence of cameras' responsivity, sensitivity, and noise analysis. Relative responsivity (a) and minimum detectable power (MDP) (b) as a function of the incident frequency band. The relative responsivity is defined as the ratio between the camera's responsivity with the low-pass filters and that with the full incident spectrum. The horizontal bars in (a) and (b) denote the spectrum-weighted standard deviation, and they are centered at the spectrum-weighted mean. Amplitude spectral density (ASD) of the noise for the IR (c) and THz (d) cameras. The frequency axis in (c) and (d) corresponds to the temporal noise spectrum derived from time-series measurements.

The responsivity for a given spectral band was calculated as the spatially integrated camera signal divided by the corresponding incident average power (see Section S1 of the Supplementary Material). Because the two detectors produce integrated output signals in different units (temperature in $^\circ\text{C}$ for the IR camera and counts for the THz camera), the *relative responsivity*, defined as the responsivity for a given spectral band normalized to the value measured under full broadband excitation, is the most relevant quantity. Fig. 2a shows the relative responsivity of the IR and THz cameras as a function of the incident spectral band. The center frequency μ_w and weighted standard deviation σ_w of each spectral band were

extracted from electro-optic sampling measurements of the incident THz spectrum (see Supplementary Material) and are depicted in Fig. 2a by the center and width of the horizontal bars.

For the THz camera, the relative responsivity falls to 50% at 1.5 THz, whereas for the IR camera, the corresponding 50% drop occurs at a higher frequency, 2.5 THz, with a steeper decline. A reduction in responsivity in the lower-THz regime is a well-known limitation of microbolometer-based detectors [16, 17], and improving performance in this spectral region remains an active area of research [7, 16]. A widely adopted approach to improve responsivity at long THz wavelengths is to increase the effective pixel area so that the absorber captures a larger fraction of the subwavelength electromagnetic field [7, 16]. Consistent with this design strategy, the difference in relative responsivity between the cameras at lower THz frequencies correlates with the larger pixel pitch of the benchmark THz camera, which is approximately twice that of the IR camera (23.5 μm versus 12 μm).

The THz frequency-dependent sensitivity was calculated as the minimum detectable power (MDP), defined as:

$$MDP = \frac{\sigma}{R} \quad \text{Eq. 1}$$

where σ is the temporal standard deviation of the detector noise, obtained from a 300-frame time-series measurement without incident radiation, and R is the responsivity. Fig. 2b shows the MDP of both detectors across the incident spectral bands. Due to the frequency-dependent responsivity, the MDP increases in

the region around ~ 1 THz by approximately three orders of magnitude for the IR camera and two orders of magnitude for the THz camera.

Under full-spectral excitation (center frequency $\mu_w = 2.9$ THz), the measured MDPs were 20 pW for the IR camera and 140 pW for the THz camera. We note that a direct comparison between these values must be treated with caution, as the cameras have different frame rates (30 Hz for the THz camera and 25 Hz for the IR camera), different readout electronics, and different signal-processing algorithms. Nonetheless, this characterization shows that the IR camera exhibited lower MDPs for the higher-frequency components of the organic crystal emission spectrum, whereas the THz camera performed better at frequencies below 1.5 THz.

While the MDP provides a practical detection limit, it relies on a temporal standard deviation that integrates the noise across the detector's entire operational bandwidth. As a result, the MDP is inherently dependent on the effective measurement bandwidth, which is determined by camera parameters such as integration time or filtering characteristics of readout electronics. To provide a more comprehensive characterization of the noise floor (and to enable a more direct comparison between different detection systems), the amplitude spectral density (ASD) of the output noise (see section S1 of the Supplementary Material) is calculated. Figs. 2c and d show that both detectors have different noise profiles. While the noise

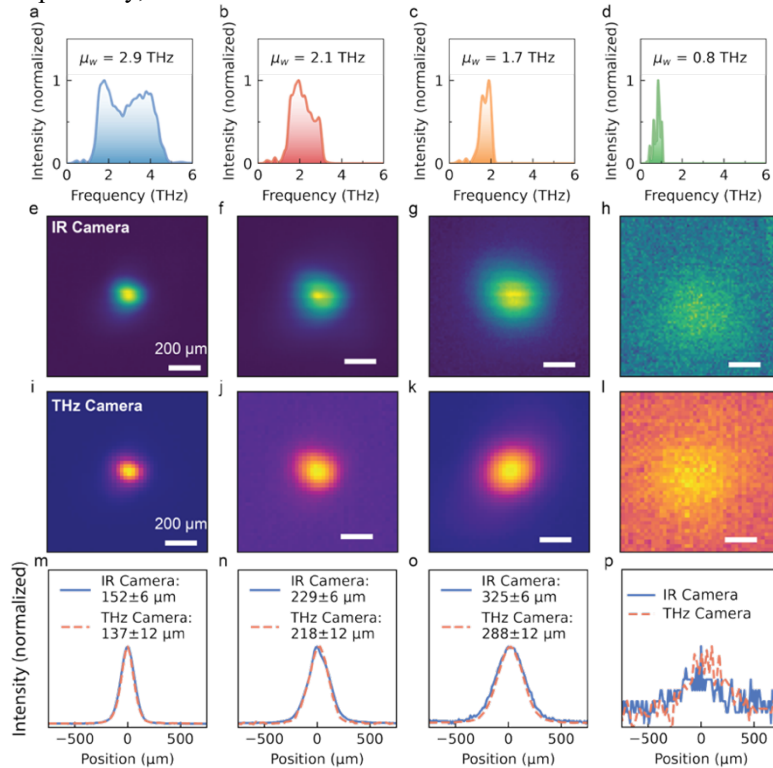


Fig. 3 Terahertz beam focus profiles across different THz spectral bands using THz lowpass filters. (a-d) Amplitude spectrum of the transmitted THz beam. The frequency bands were controlled using low-pass THz filters with cutoff frequencies of 10, 3.0, 2.0, and 1.0 THz, respectively (see Supplementary Material S1). The central frequency (weighted mean) calculated from the measured THz waveform is indicated in each panel. Images (e-l) and cross-cuts (m-p) of the THz beam profile recorded with the IR (e-h) and THz (i-l) cameras. All scale bars correspond to 200 μm .

from the IR camera is dominated by $1/f$ (pink) noise, the noise from the THz camera contains peaks in the region below 3 Hz. In contrast, for frequencies above 3 Hz, the THz camera ASD is flatter, indicating a more stable noise floor.

As microbolometric detectors exhibit a frequency-dependent cutoff in their spectral responsivity (and sensitivity), beam-profiling measurements performed with broadband THz radiation may, in principle, underestimate the true focal spot size by preferentially weighting higher-frequency components.

To isolate the magnitude of this effect (for profiling broadband THz emission from organic crystals), we performed numerical simulations using the experimentally measured spectral responsivities of both cameras. The purpose of this calculation is not to reproduce the absolute measured focal spot size—which depends on optical alignment, aberrations, and the wavelength-dependent initial beam waist—but rather to quantify the bias introduced solely by detector spectral weighting. Starting from the relative responsivity curves shown in Fig. 2a, continuous responsivity functions were constructed and applied to the measured DSTMS emission spectrum. Each spectral component was then propagated through the focusing geometry using a Gaussian beam model, with the same optical input assumed for both detectors. In this way, any difference in the reconstructed beam profile arises exclusively from the detectors' spectral responsivity. Full details of the numerical procedure are provided in Section S3 of the Supplementary Material.

Using a spectrally flat (ideal) responsivity as a reference, the reconstructed focal width is 120 μm . When the measured spectral responsivities of the THz and IR cameras are applied, the corresponding reconstructed widths become 116 μm and 112 μm , respectively, corresponding to deviations below 7% relative to the flat-responsivity case. These small relative differences indicate that spectral roll-off alone does not introduce a significant distortion in the reconstructed beam width for broadband spectra dominated by frequencies above 2 THz.

To further investigate the dependence of the observed beam profile on frequency, measurements are made as the incident THz spectrum is systematically shifted toward lower frequencies using a series of low-pass THz filters. The resulting beam profiles for the different spectral bands are shown in Fig. 3. The amplitude spectra for the different filter settings are displayed in the top row, and the corresponding measurements made with the IR and THz cameras for that particular spectral range are shown below. For the lowest-frequency band centered at 0.8 THz (Figs. 3d, 3h, and 3l), the DSTMS emitter was replaced with a PNPA organic crystal [15], which has a higher THz conversion efficiency below 1.5 THz.

As the spectral content is shifted toward lower frequencies, the effective beam size increases due to the larger diffraction-limited spot size at longer wavelengths. Moreover, at higher frequencies, the acquired profiles exhibit enhanced signal-to-noise ratios, yielding well-resolved intensity distributions. The performance degrades for both cameras at the lowest frequency ($\mu_w = 0.8$ THz, Figs. 3h and 3l), where the power is lower (see

Supplementary Table 2). The loss in signal-to-noise and detected intensity is primarily due to the lower responsivity of both cameras at these frequencies.

A quantitative comparison of the measured beam widths clarifies the impact of spectral effects on beam profiling. For spectral bands centered at $\mu_w = 2.9$ THz and $\mu_w = 2.1$ THz, the FWHM measured by the IR and THz cameras agrees within the spatial sampling uncertainty set by the respective pixel pitches. In contrast, for the spectral band centered at $\mu_w = 1.7$ THz, the IR camera yields a beam diameter that is approximately 11% larger than that measured with the THz camera, exceeding the expected sampling-related uncertainty.

Notably, this discrepancy cannot be explained by the reduced responsivity at lower frequencies, as this would preferentially weight higher-frequency components and lead to a smaller, rather than larger, measured beam diameter. The observed broadening when $\mu_w = 1.7$ THz may instead be attributed to a modest contribution from pixel-to-pixel cross-talk in the IR camera. Such thermal or radiative cross-talk, arising from non-perfect thermal or electromagnetic isolation between neighboring pixels, is expected to become more pronounced when operating near the lower-frequency limit of the device [18]. Importantly, a discrepancy exceeding the spatial sampling uncertainty (set by the respective pixel pitches) was observed only for spectral bands below 2 THz, and therefore does not affect the overall ability of the IR camera to accurately reconstruct broadband THz beams. At the lowest spectral band ($\mu_w = 0.8$ THz), the detected signal is substantially reduced due to the diminished responsivity of both cameras, resulting in a low signal-to-noise ratio. At this frequency, a reliable extraction of the FWHM is not possible, and no quantitative comparison of beam diameters is reported.

While the previous measurements are made to characterize the cameras under broadband pulsed THz excitation, many practical applications, especially imaging, rely on CW and quasi-CW THz sources. Therefore, in a second set of measurements, the performance of the IR camera under quasi-CW conditions was evaluated. An on-chip quantum cascade laser (QCL) providing a stable, multimode output at approximately 3 THz (bandwidth: ~ 250 GHz FWHM) was used for these tests. More details on the QCL, including emission spectrum and operation characteristics, can be found in ref. [19] where the same QCL platform used in this work is described and characterized.

The QCL itself is pulsed at a 200 kHz repetition rate, with a 10% duty cycle, and this pulse train is then gated at 105 Hz using a 50% duty cycle to match the camera's integration time. A schematic of the experiment and the measured beam profiles are shown in Fig. 4. The profiles were acquired at an incident THz average power attenuated to below 2 μW . Consistent with the results obtained with the broadband THz excitation, the IR camera produced a beam profile of the QCL that closely matched the profile from the THz camera. Specifically, the horizontal FWHM spot size measured with the IR camera was $141 \pm 6 \mu\text{m}$, compared to $139 \pm 12 \mu\text{m}$ for the THz camera. Near-perfect agreement under these conditions further confirms

the suitability of the IR microbolometer for accurate THz beam profiling under both pulsed broadband and quasi-CW narrowband excitation.

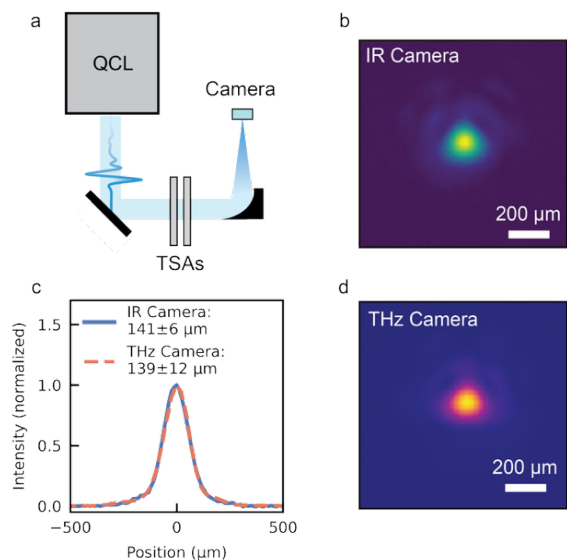


Fig. 4 Quasi-Continuous-Wave THz imaging with a quantum cascade laser (QCL). (a) Illustration of the experimental setup used to test the cameras under a quasi-CW regime. A QCL was used to generate a beam centered at 3 THz, which was focused onto the camera's detector. The power was controlled with THz silicon attenuators (TSAs) placed in series. (b) Image of intensity profile in the IR camera. (c) Horizontal cross-cut of the beam profiles from (b) and (d), after background subtraction. (d) Beam image recorded with the THz camera. Scale bars in (b) and (d) are 200 μm.

In summary, relatively inexpensive, IR microbolometric cameras can be used for beam profiling with similar performance to that of a specialized THz camera. For broadband THz radiation from organic crystals, the IR camera reproduced the beam profile with deviations below ~6%. Notably, this discrepancy corresponds to less than the sensor's 12 μm pixel pitch, suggesting that the observed difference is limited primarily by spatial sampling rather than detector sensitivity. Furthermore, simulations incorporating the measured spectral responsivity indicate that the low-frequency roll-off introduces only minor distortions (<7%). Measurements using a 3-THz on-chip QCL provide additional agreement between the two systems, yielding spot-size differences of only ~1.3%. Overall, this work shows that off-the-shelf IR microbolometric cameras can be used as reliable and accurate instruments for THz beam diagnostics, establishing these cameras as a standard tool for routine alignment and imaging in terahertz science and technology.

ACKNOWLEDGMENT

The authors express their gratitude to the PSI-LNO GL group for their support during the experiments.

REFERENCES

- [1] C. Roundy, "The importance of beam profile," *Physics World*, vol. 3, no. 7, p. 65, 1990.
- [2] R. Hain, C. J. Kähler, and C. Tropea, "Comparison of CCD, CMOS and intensified cameras," *Exp. Fluids*, vol. 42, no. 3, pp. 403-411, 2007.
- [3] H. Guerboukha, K. Nallappan, and M. Skorobogatiy, "Toward real-time terahertz imaging," *Advances in Optics and Photonics*, vol. 10, no. 4, pp. 843-938, 2018.
- [4] A. Rogalski and F. Sizov, "Terahertz detectors and focal plane arrays," *Opto-Electronics Review*, vol. 19, no. 3, pp. 346-404, 2011/09/01 2011, doi: 10.2478/s11772-011-0033-3.
- [5] Z. Bielecki, J. Mikolajczyk, and J. Wojtas, "A Review of Thermal Detectors of THz Radiation Operated at Room Temperature," *Sensors*, vol. 24, no. 21, p. 6784, 2024. [Online]. Available: <https://www.mdpi.com/1424-8220/24/21/6784>.
- [6] M. J. Coppinger, N. A. Sustersic, J. Kolodzey, and T. H. Allik, "Sensitivity of a vanadium oxide uncooled microbolometer array for terahertz imaging," *Optical Engineering*, vol. 50, no. 5, pp. 053206-053206-5, 2011.
- [7] N. Oda *et al.*, "Microbolometer Terahertz Focal Plane Array and Camera with Improved Sensitivity in the Sub-Terahertz Region," *Journal of Infrared, Millimeter, and Terahertz Waves*, vol. 36, no. 10, pp. 947-960, 2015/10/01 2015, doi: 10.1007/s10762-015-0184-2.
- [8] P. Zolliker, M. Shalaby, E. Söllinger, E. Mavrona, and E. Hack, "Real-Time High Resolution THz Imaging with a Fiber-Coupled Photo Conductive Antenna and an Uncooled Microbolometer Camera," *Sensors*, vol. 21, no. 11, p. 3757, 2021. [Online]. Available: <https://www.mdpi.com/1424-8220/21/11/3757>.
- [9] R. Lewis, "A review of terahertz detectors," *J. Phys. D: Appl. Phys.*, vol. 52, no. 43, p. 433001, 2019.
- [10] R. Gade and T. B. Moeslund, "Thermal cameras and applications: a survey," *Machine Vision and Applications*, vol. 25, no. 1, pp. 245-262, 2014/01/01 2014, doi: 10.1007/s00138-013-0570-5.
- [11] F. Blanchard, J. E. Nkeck, D. Matte, R. Nechache, and D. G. Cooke, "A Low-Cost Terahertz Camera," *Applied Sciences*, vol. 9, no. 12, p. 2531, 2019. [Online]. Available: <https://www.mdpi.com/2076-3417/9/12/2531>.
- [12] A. Ravagli, M. Naftaly, C. Craig, E. Weatherby, and D. W. Hewak, "Dielectric and structural characterisation of chalcogenide glasses via terahertz time-domain spectroscopy," *Opt. Mater.*, vol. 69, pp. 339-343, 2017/07/01/ 2017, doi: <https://doi.org/10.1016/j.optmat.2017.04.057>.
- [13] A. Shakhmin, V. Gerasimova, S. Musikhin, and G. Kropotov, "Terahertz Spectroscopy of Germanium with Different Doping Levels," *Crystals*, vol. 15, no. 10, p. 861, 2025.
- [14] Z. Yang *et al.*, "Large-Size Bulk and Thin-Film Stilbazolium-Salt Single Crystals for Nonlinear Optics and THz Generation," *Adv. Funct. Mater.*, vol. 17, no. 13, pp. 2018-2023, 2007, doi: <https://doi.org/10.1002/adfm.200601117>.
- [15] C. Rader *et al.*, "A New Standard in High-Field Terahertz Generation: the Organic Nonlinear Optical Crystal PNPA," *ACS Photonics*, vol. 9, no. 11, pp. 3720-3726, 2022/11/16 2022, doi: 10.1021/acsp Photonics.2c01336.
- [16] F. Simoens and J. Meilhan, "Terahertz real-time imaging uncooled array based on antenna-and cavity-coupled bolometers," *Philosophical Transactions of the Royal Society A: Mathematical, Physical and Engineering Sciences*, vol. 372, no. 2012, p. 20130111, 2014.
- [17] F. Sizov, "Terahertz radiation detectors: the state-of-the-art," *Semicond. Sci. Technol.*, vol. 33, no. 12, p. 123001, 2018.
- [18] S. Fusetto, A. Aprile, P. Malcovati, and E. Bonizzoni, "Readout IC architectures and strategies for uncooled micro-bolometers infrared focal plane arrays: A review," *Sensors*, vol. 23, no. 5, p. 2727, 2023.
- [19] U. Senica *et al.*, "Planarized THz quantum cascade lasers for broadband coherent photonics," *Light Sci. Appl.*, vol. 11, no. 1, p. 347, 2022.

Supplementary Material for

Profiling THz Beams With Off-Label Use of Infrared Microbolometric Cameras

Gabriel Nagamine,¹ Carlo Vicario,² Tariq Leinen,¹ Guy Matmon,² Marco Raffa,³ Mattias Beck,³
Giacomo Scaliari,³ Adrian L. Cavalieri,^{1,2} Flavio Giorgianni^{1,2}

¹*Institute of Applied Physics, University of Bern, CH-3012 Bern, Switzerland*

²*Paul Scherrer Institute, CH-5232 Villigen-PSI, Switzerland*

³*Institute for Quantum Electronics, Department of Physics, ETH Zürich, CH-8093 Zurich, Switzerland*

S1. Experimental Methods

Beam Profiling for Pulsed Excitation. The experimental setup for the beam profiling measurements is illustrated in Figure 1a from the main text. In short, a 1 kHz Ti:Sapphire laser, coupled with an optical parametric amplifier, was used to pump an organic crystal to generate collimated THz radiation. The pump wavelength was ~ 1350 nm, for an efficient THz generation through optical rectification. In this study, all measurements in the pulsed regime were performed by pumping a DSTMS organic crystal,^{S1} except for the measurements shown in Figures 3d, h, and l of the main text, where we used PNPA^{S2} due to its enhanced emission at lower THz frequencies. To avoid leakage from the pump, a set of two THz low-pass filters with a cutoff frequency of 20 THz combined with one filter with a cutoff frequency of 10 THz was positioned after the organic crystal. To generate a tight focus, the beam was expanded and then focused using a series of unprotected gold off-axis parabolic mirrors. The focal distances of the parabolic mirrors were, in sequence: 1, 6, and 2 inches. The focused beam was then imaged by a Mini2PlusV2 infra-red (IR) camera from HIKMICRO and by a T0831 THz camera from NEC. For simplicity, in the main text, we refer to these cameras as “IR” and “THz” cameras, respectively. To measure power, a THZ5I-BL-BNC from Gentec was used. For the responsivity measurements, the power was controlled by varying the angle between two THz polarizers in series.

IR Camera Data Extraction and Background Subtraction. The IR camera data were stored as radiometric files, containing the full per-pixel temperature information in addition to the RGB

Corresponding Authors

E-mails: flavio.giorgianni@unibe.ch, gabriel.nagaminegomez@unibe.ch

visualization. The temperature matrix was extracted using the analysis software provided by the manufacturer at the native spatial resolution of the detector array. Background correction was performed by acquiring two consecutive images, alternatively blocking and unblocking the THz radiation. The background was then subtracted from the signal in a post-processing step using custom-written Python scripts.

Characterization of the Polarization Dependence of the Cameras' Response. To assess the isotropic response of the detectors, we have performed measurements with both cameras in horizontal and vertical orientations, while the THz light remained vertically polarized in relation to the laboratory frame. The incident THz power and linear polarization were kept constant for both configurations, and the full THz beam profile was recorded in each case. The integrated signal was then calculated for each orientation. The results are summarized in the Supplementary Table 1.

Supplementary Table 1. Summary of results for isotropic response characterization.

	Vertical Orientation Integrated Signal	Horizontal Orientation Integrated Signal	Relative Signal Difference (%)
IR Camera	5171 °C	5156 °C	0.3
THz Camera	75049 counts	74832 counts	0.3

Computation of the Amplitude Spectral Density. The amplitude spectral density (ASD) of the noise floor was obtained from the square root of the power spectral density (PSD) function. The PSD was calculated from a time series containing 300 frames, with the camera shutter blocked. The calculation was performed using the Welch's method^{S3} implemented via the scipy signal^{S4} library. The resulting PSD function was obtained after averaging over a 100x100-pixel block. Figure 2a and b from the main text show the obtained ASD functions for the IR and THz cameras, respectively.

Quasi-continuous-Wave Excitation with a Quantum Cascade Laser. For continuous-wave illumination (CW), a specifically designed on-chip quantum cascade laser (QCL) was used to generate THz radiation at a frequency of 3 THz with 250 GHz bandwidth FWHM^{S5}. The on-chip QCL was cooled at temperatures below 20 K, and it was driven at a 200 kHz repetition rate, with a 10% duty cycle. The emitted radiation was collected with an off-axis parabolic mirror and then refocused on the detector. A 6 THz low-pass filter was used to cut the ambient background. This micro-pulse train was then gated at 105 Hz using a 50% duty cycle. The incident power on the detector was $< 2 \mu\text{W}$, corresponding to a peak irradiance $< 13 \text{ mW}/\text{cm}^2$.

Spectral Band Control Using Low-Pass THz Filter. To vary the incident spectral band, a series of low-pass THz filters supplied by QMC Instruments Ltd. was used. For the spectral characterization, we performed electrooptical sampling (EOS).^{S6} The experimental setup for EOS characterization is shown in Figure S2. The obtained THz field in time is shown in Figure S1 b-e, while the respective fields in the frequency domain are shown in Figure S2. The cutoff frequencies for the THz filters were 10, 3, 2, and 1 THz. We identify each field based on the weighted mean (μ_w) as done in the main text. For all fields, a DSTMS^{S1} crystal was used to generate THz, except for the one centered at 0.8 THz, where we used PNPA^{S2} for more efficient THz generation.

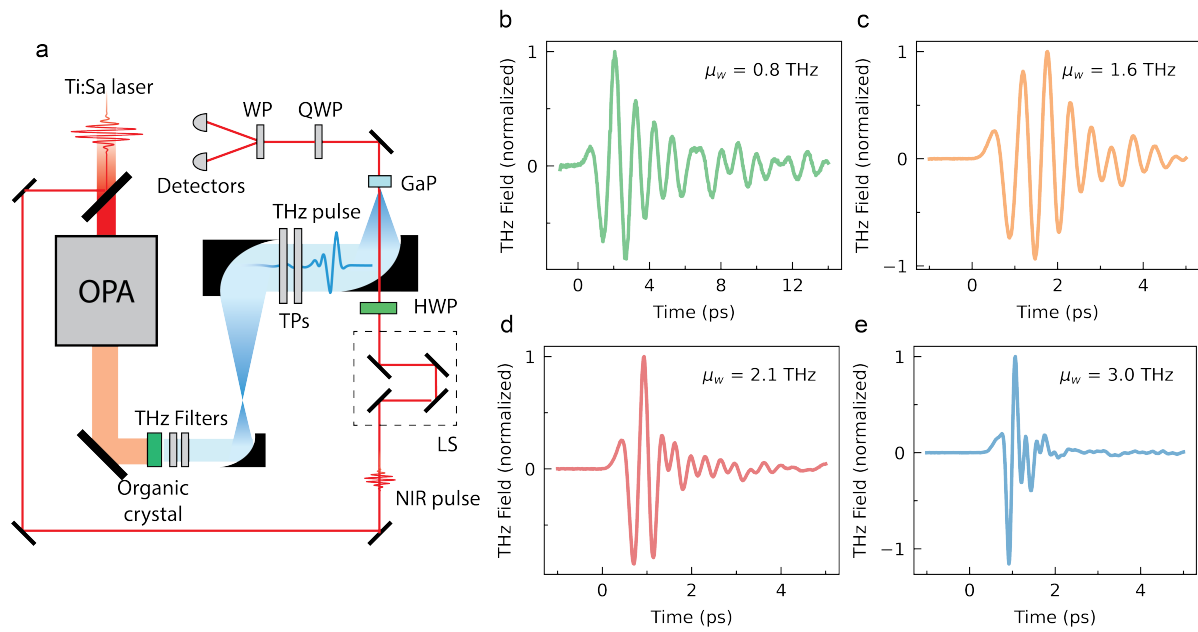


Figure S1. Electro Optical Sampling for THz Field Characterization. (a) Illustration of the setup used for electro-optical sampling (EOS). LS: linear stage, HWP: half-wave plate, TPs: THz polarizers, QWP: quarter-wave plate, WP: Wollaston prism. (b-e) THz field in the time domain, obtained from EOS. The timetraces were obtained using low-pass THz filters with cutoff frequencies of 1 THz (b), 2 THz (c), 3 THz (d), and 10 THz (e). The panels show the weighted mean frequency (μ_w), obtained from the data in the frequency domain.

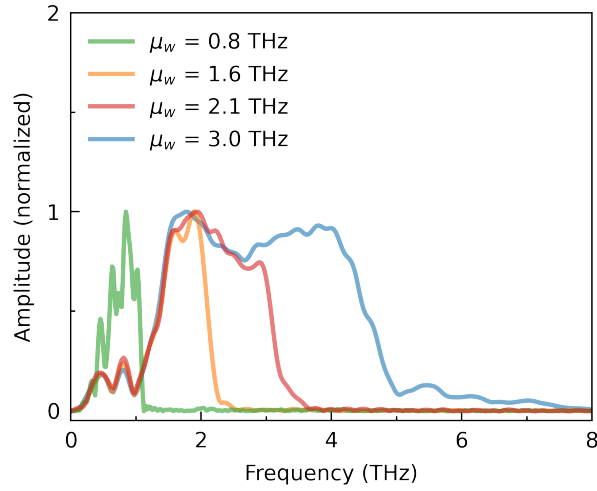


Figure S2. THz Spectra Varying Incident Frequency Band. The spectra were obtained from a fast Fourier transform of the data shown in Figure S1(b-e). To control the incident frequency band, we used low-pass THz filters with cutoff frequencies of 1 THz, 2 THz, 3 THz, and 10 THz, generating spectra with weighted means of 0.8, 1.6, 2.1, and 3.0 THz, respectively.

Calculation of the Relative Responsivity

The responsivity at a given center frequency f can be calculated by the following equation:

$$R_f = \frac{S_f}{P_f}, \quad \text{S1}$$

where S and P refer to the measured signal and power, respectively. The signal was measured as the integrated intensity over the beam profile, and the parameters used for the calculation are listed in Supplementary Table 2. The normalized responsivity was calculated by dividing R_f by the responsivity obtained with full spectral excitation (weighted mean frequency of 2.9 THz).

Supplementary Table 2. Parameters used for calculating the responsivity.

Weighted mean frequency (THz)	IR camera integrated signal (°C)	THz camera integrated signal (counts)	Incident Power (μW)
0.8	40.4	8606	9.05
1.7	3325.5	249028	20.9
2.1	460.8	29638	1.0
2.9	8990.9	143760	3.8

Determination of the Spatial THz Beam FWHM

The spatial full width at half maximum (FWHM) of the focused THz beam was extracted from one-dimensional horizontal intensity profiles obtained from the beam images. For each profile, the half-maximum level was defined as half of the peak intensity of the spatial distribution. The positions at which the intensity crossed this level were determined using linear interpolation between adjacent data points surrounding each crossing. The FWHM was then calculated as the distance between the left and right interpolated half-maximum positions.

S2. Simulation of Beam-Profile Distortion from Spectrally-Dependent Responsivity

To quantify the distortions caused by the spectrally-dependent responsivity on beam profiling, we first extract a continuous responsivity function from the data shown in Figure 2 of the main text. To do so, we interpolated the data using a cubic Hermite interpolator (PchipInterpolator from SciPy^{S4}). Then, the square root of the interpolated responsivity was applied to the DSTMS THz emission spectrum (blue curve from Figure S2) to generate a responsivity-weighted electric field spectrum. The extracted square root of the interpolated responsivity for both cameras is shown in Figure S3.

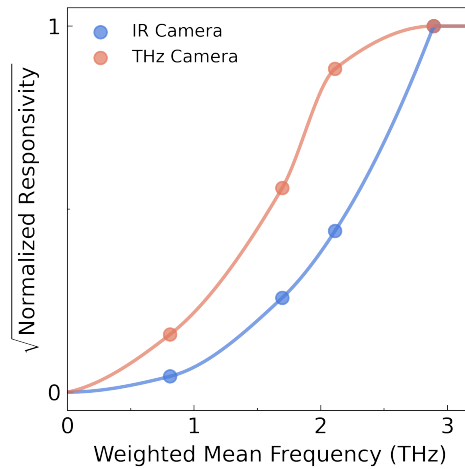


Figure S3. Square root of the relative responsivity and interpolated curves. The data were extracted for the IR (blue) and THz (red) cameras using the procedure described in section S1.

The responsivity-weighted electric-field spectrum was then used to simulate the spatial distribution of the field intensity at the focus of the parabolic mirror. The simulation assumes that each spectral component propagates as a Gaussian beam, and the final beam profile will be the sum of the profiles from each spectral component. The Gaussian beam waist at the focus of the parabola is given by:

$$w(v) = \frac{cf}{v\pi w_{in}}, \quad \text{S2}$$

where ν , c , f , w_{in} , are the THz frequency, speed of light, focal distance, and beam waist of the beam before the parabolic mirror. The corresponding intensity profile of each spectral component is given by:

$$I(\nu, r) = \frac{2|E(\nu)|^2}{\pi w(\nu)^2} \exp\left(-\frac{2r^2}{w(\nu)^2}\right) \quad S3$$

Where $E(\nu)$ is the responsivity weighted electric field, and $r = \sqrt{x^2 + y^2}$. The full detected profile is then the integral over all spectral components:

$$I_{total}(x, y) = \int I(\nu, \sqrt{x^2 + y^2}) d\nu. \quad S4$$

This procedure was implemented numerically using a 2D spatial grid and trapezoidal integration over the frequency axis.

Supplementary References

(S1) Yang, Z.; Mutter, L.; Stillhart, M.; Ruiz, B.; Aravazhi, S.; Jazbinsek, M.; Schneider, A.; Gramlich, V.; Günter, P. Large-Size Bulk and Thin-Film Stilbazolium-Salt Single Crystals for Nonlinear Optics and THz Generation. *Adv. Funct. Mater.* **2007**, *17*, 2018-2023.

(S2) Rader, C.; Zaccardi, Z. B.; Ho, S.-H. E.; Harrell, K. G.; Petersen, P. K.; Nielson, M. F.; Stephan, H.; Green, N. K.; Ludlow, D. J. H.; Lutz, M. J.; Smith, S. J.; Michaelis, D. J.; Johnson, J. A. A New Standard in High-Field Terahertz Generation: the Organic Nonlinear Optical Crystal PNPA. *ACS Photonics* **2022**, *9*, 3720-3726.

(S3) Welch, P. The use of fast Fourier transform for the estimation of power spectra: A method based on time averaging over short, modified periodograms. *IEEE Transactions on audio and electroacoustics* **1967**, *15*, 70-73.

(S4) Virtanen, P.; Gommers, R.; Oliphant, T. E.; Haberland, M.; Reddy, T.; Cournapeau, D.; Burovski, E.; Peterson, P.; Weckesser, W.; Bright, J.; van der Walt, S. J.; Brett, M.; Wilson, J.; Millman, K. J.; Mayorov, N.; Nelson, A. R. J.; Jones, E.; Kern, R.; Larson, E.; Carey, C. J.; Polat, İ.; Feng, Y.; Moore, E. W.; VanderPlas, J.; Laxalde, D.; Perktold, J.; Cimrman, R.; Henriksen, I.; Quintero, E. A.; Harris, C. R.; Archibald, A. M.; Ribeiro, A. H.; Pedregosa, F.; van Mulbregt, P.; Vijaykumar, A.; Bardelli, A. P.; Rothberg, A.; Hilboll, A.; Kloeckner, A.; Scopatz, A.; Lee, A.; Rokem, A.; Woods, C. N.; Fulton, C.; Masson, C.; Häggström, C.; Fitzgerald, C.; Nicholson, D. A.; Hagen, D. R.; Pasechnik, D. V.; Olivetti, E.; Martin, E.; Wieser, E.; Silva, F.; Lenders, F.; Wilhelm, F.; Young, G.; Price, G. A.; Ingold, G.-L.; Allen, G. E.; Lee, G. R.; Audren, H.; Probst, I.; Dietrich, J. P.; Silterra, J.; Webber, J. T.; Slavič, J.; Nothman, J.; Buchner, J.; Kulick, J.; Schönberger, J. L.; de Miranda Cardoso, J. V.; Reimer, J.; Harrington, J.; Rodríguez, J. L. C.; Nunez-Iglesias, J.; Kuczynski, J.; Tritz, K.; Thoma, M.; Newville, M.; Kümmerer, M.; Bolingbroke, M.; Tartre, M.; Pak, M.; Smith, N. J.; Nowaczyk, N.; Shebanov, N.; Pavlyk, O.; Brodtkorb, P. A.; Lee, P.; McGibbon, R. T.; Feldbauer, R.; Lewis, S.; Tygier, S.; Sievert, S.; Vigna, S.; Peterson, S.; More, S.; Pudlik, T.; Oshima, T.; Pingel, T. J.; Robitaille, T. P.; Spura, T.; Jones, T. R.; Cera, T.; Leslie, T.; Zito, T.; Krauss, T.; Upadhyay, U.; Halchenko, Y. O.; Vázquez-Baeza, Y.; SciPy, C. SciPy 1.0: fundamental algorithms for scientific computing in Python. *Nature Methods* **2020**, *17*, 261-272.

(S5) Senica, U.; Forrer, A.; Olariu, T.; Micheletti, P.; Cibella, S.; Torrioli, G.; Beck, M.; Faist, J.; Scalari, G. Planarized THz quantum cascade lasers for broadband coherent photonics. *Light Sci. Appl.* **2022**, *11*, 347.

(S6) Wu, Q.; Zhang, X.-C. Free-space electro-optic sampling of terahertz beams. *Appl. Phys. Lett.* **1995**, *67*, 3523-3525.